Effect of flagellar beating pattern on sperm rheotaxis and boundary-dependent navigation

Meisam Zaferani[1], Farhad Javi[1], Amir Mokhtare[1], Alireza Abbaspourrad[1]†

[1] Department of Food Science, College of Agriculture and Life Sciences, Cornell University,

Ithaca, NY, 14850, USA

† Corresponding author: alireza@cornell.edu

Abstract

The study of navigational mechanisms used by mammalian sperm inside a microenvironment yields better understanding of sperm locomotion during the insemination process, which aids in the design of tools for overcoming infertility. Near- and far-field hydrodynamic interactions with nearby boundaries and rheotaxis are known to be some of the steering strategies that keep sperm on the correct path toward the egg. However, it is not known how the beating patterns of sperm may influence these navigational strategies. In this study, we investigate the effect of flagellar beating pattern on navigation of sperm cells both theoretically and experimentally using a two-step approach. We first isolate bovine sperm based on their rheotactic behavior in a zone with quiescent medium using a microfluidic system. This step ensures that the swimmers are able to navigate upstream and have motilities higher than a selected value, even though they feature various flagellar beating patterns. We then explore the flagellar beating pattern of these isolated sperm and their subsequent influence on boundary-dependent navigation. Our findings indicate that rheotaxis enables sperm to navigate upstream even in the presence of circular motion in their motility, whereas boundary-dependent navigation is more sensitive to the circular motion and selects for progressive motility. This finding may explain the clinical importance of progressive

23 motility in semen samples for fertility, as the flow of mucus may not be sufficiently strong to orient

24 the sperm cells throughout the process of insemination.

25 **Keywords:** Mammalian sperm | Navigation | Rheotaxis | Boundary-dependent navigation |

26 Progressive motility

27 **Significance**

28 Finding the egg and moving toward it while traversing the complex structure of the female

29 reproductive tract is necessary for mammalian sperm. Previous studies have shown how sperm use

30 navigational steering mechanisms that are based on swimming upstream (i.e. rheotaxis) and along

31 the boundaries of the female reproductive tract. We demonstrate that the performance of theses

32 navigational mechanisms is associated with the primary characteristics of sperm motility. In fact,

33 sperm rheotaxis is more sensitive to the motility and thus average velocity of sperm while

34 navigation via rigid boundaries is more sensitive to the flagellar beating pattern and selects for

35 symmetric beating. Our results can be expanded to other autonomous microswimmers and their

36 subsequent navigation mechanisms.

37

38

39

40

41

42

43

Introduction

For successful fertilization, sperm cells must traverse the distance between the location of semen deposition and the egg (1). During this transport, sperm cells require navigational mechanisms to find the correct direction in which to move (2). These navigational mechanisms rely on external stimuli, including chemical (3–5), thermal (6), and fluid mechanical (7–9) clues, which vary among different species. For instance, marine plants and animals (10, 11) release their gametes into the sea, where chemotactic behavior is observed (4, 11–13). Strikingly, the role of this chemical communication observed in marine invertebrate sperm (which is reminiscent of bacterial chemotaxis (14)) is uncertain in the navigation of mammalian sperm (13, 15–19). In contrast, *in vitro/vivo* evidence suggests that the navigation of mammalian sperm within the female reproductive tract depends more on fluid mechanical clues rather than other external stimuli (2, 7, 9, 20, 21).

The navigational system of mammalian sperm to find the correct path toward the fertilization site includes boundary-dependent navigation (20–22) and upstream swimming behavior, known as "rheotaxis" (8, 23, 24). Based on extensive studies carried out previously, the characteristics of rheotactic behavior are determined by the external flow in which the sperm are swimming, and a minimum shear rate is required for upstream swimming to emerge (23). However, boundary-dependent navigation that relies upon the hydrodynamic interactions of the swimmer with rigid walls, as well as self-propulsion and steric repulsion of sperm cells (25), is independent of the external flow and exists even in a quiescent medium. In fact, boundary-dependent navigation consists of a far-field hydrodynamic attraction of the sperm toward nearby walls (26–29), such as those of the female reproductive tract, followed by stably swimming along these boundaries (20, 21, 37, 22, 30–36). Berke et al. (27) proposed a dipole swimmer model that

3

67   describes the attraction of sperm as a microswimmer with absolute progressive motility toward

68   rigid boundaries at distances far enough from the boundaries (i.e., the far-field approximation). At

69   close distances, swimming along boundaries is observed ubiquitously among microswimmers and

70   Denissenko et al. (20) have demonstrated this boundary-following motion in the sperm using a

71   microchannel and proposed it as a navigational mechanism.

72   Although sperm rheotaxis and boundary-dependent navigation have been studied, the

73   intriguing unanswered question is how does the flagellar beating pattern affect these navigational

74   mechanisms? Since sperm cells in a population feature both progressive and non-progressive

75   motility, answering this question reveals the optimum motility mode required for sperm to be

76   steered by such navigational mechanisms. Previous studies have explored sperm flagellar beating

77   and its hydrodynamic interaction with rigid boundaries (20, 38, 39). However, such studies have

78   not revealed the role of the beating pattern in sperm navigation comprehensively because they

79   have not considered sperm rheotaxis. The dynamic flow of mucus within the female reproductive

80   tract necessitates studying the effect of the flagellar beating pattern on sperm rheotaxis and

81   boundary-dependent navigation concurrently. Therefore, controlled experimentation to quantify

82   the effect of the beating pattern on different sperm navigational mechanisms is desirable. However,

83   at shear rates at which upstream swimming occurs, characterizing the role of the beating pattern

84   in the sperm locomotion and subsequent interactions is challenging as the flow overcomes all the

85   non-upstream components of the motion. Furthermore, decoupling the contribution of the flow

86   and the beating in the sperm motion is experimentally challenging in itself.

87   In this study, we investigate the navigation of sperm cells both theoretically and

88   experimentally using a two-step approach. The first step is to isolate the sperm cells in a reservoir

89   with quiescent medium via a rheotaxis-based method using a microfluidic system (40). This

90 microfluidic rheotaxis-based isolation step ensures that all sperm cells navigate upstream via

91 rheotaxis and have motilities higher than a selected threshold value, even though they feature

92 various flagellar beating patterns. The second step is to study the tail beating of these sperm and

93 their subsequent boundary-dependent navigation in a reservoir with quiescent medium to

94 determine the influence of the tail beating pattern on this navigational mechanism. For this second

95 step, we use phase contrast microscopy, cell tracking, resistive force theory (41), lubrication

96 approximation (42), and finite element method simulation. This two-step approach bypasses the

97 challenges associated with studying the flagellar beating pattern in simple shear flow yet enables

98 us to investigate sperm rheotaxis and boundary-dependent navigation concurrently.

99 **Results and Discussion**

100 To characterize the sperm flagellar beating patterns, we first isolated motile swimmers

101 within a zone of a microfluidic chip filled with Tyrode albumin lactate pyruvate (TALP) medium

102 using a rheotaxis-based method (40). For more details about this isolation technique, please see

103 the Methods section. The movement of the motile sperm inside the microfluidic zone filled with

104 quiescent medium can be seen in Movie S1, which shows that sperm with symmetric beating

105 patterns move with progressive motion, whereas those with asymmetry in their beating patterns,

106 i.e., one part of the flagellum consistently bends more significantly to one side, swim in circular

107 paths. Interestingly, all these sperm have navigated upstream via rheotaxis even though they

108 feature different beating patterns ranging from symmetric to asymmetric. In addition, the velocity

109 of the average path (VAP) in the separated sample is higher than a threshold value (VAP $\geq$

110 53.2 μm/s). In our previous study (40), we demonstrated that this minimum threshold is tunable

111 via the injection rate. The various flagellar beating patterns and the tunable minimum VAP in the

112   separated samples indicate that sperm rheotaxis is more sensitive to VAP and thus motility itself

113   rather than the pattern of the flagellar beating.

114   The asymmetric flagellar beating pattern and pathway of these circular-swimming sperm

115   were captured using phase-contrast microscopy, as shown in Fig. 1(a) and (b). Fig. 1(c)

116   demonstrates the trajectories of nine other sperm exhibiting such circular motion, in which the

117   centers of these circular paths move randomly over time. Initial observations also suggest the non-

118   significant influence of the wall on the motion of the sperm with non-progressive motility

119   compared to that of the progressive ones. In fact, due to near-wall hydrodynamic interactions,

120   when sperm with symmetric beating patterns and thus progressive motility encounter the side wall,

121   they begin to swim parallel along it (indicated by the blue line in Fig. 1(d)). Meanwhile, the sperm

122   with asymmetric beating either retain their circular trajectory (indicated by the red line in Fig. 1(d))

123   or return to the circular trajectory after partially following the wall.

124   To quantitatively describe the asymmetric beating pattern, circular motion, and

125   hydrodynamic interactions of the sperm, we first quantified the correlation between the asymmetry

126   in the beating and the circular motion. It has been observed that in a quiescent medium, sperm

127   (similar to *E. coli*) swim in proximity to surfaces and in large circles so that the rotation axis is

128   perpendicular to the surface even if the motion produced by the flagellum is progressive. Tung et

129   al. (23) and Lauga et al. (43) attributed this circular motion to the swimmer's hydrodynamic

130   interactions with the surface, as the head and tail of bacteria rotate counter clockwise and clockwise

131   (or vice versa), respectively (44–46), while sperm exhibit self-rolling motion. This self-rolling

132   motion consists of the sperm head and tail rotating in the x-z plane with Ω_R, as indicated in Fig.

133   1(E). This rotation in the sperm head and tail generates a subsequent angular velocity that leads to

134   the microswimmer swimming in circles in the x-y plane. Otherwise, in the absence of the self-

135   rolling motion, a progressive sperm cell does not experience torque and swims progressively. We

136   used phase-contrast microscopy (47) to examine whether the sperm in our experiment exhibit this

137   self-rolling motion, in which the paddle-shaped head of the bovine sperm twinkles as it flips as

138   demonstrated in Fig. 1(F). As can be seen in Fig. 1(b) and (c), no twinkling was observed in the

139   sperm with intrinsic circular motion. Therefore, the hydrodynamic interactions with the top (or

140   bottom) surface of the microfluidic chip are not responsible for the circular motion we observe,

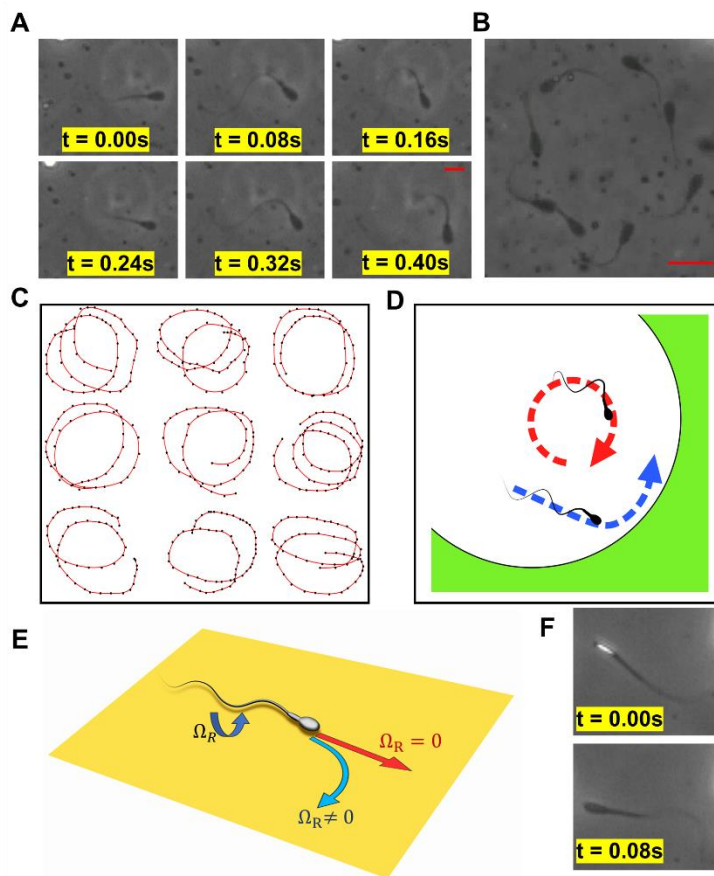141   indicating the circular motion is solely due to intrinsic asymmetry in the flagellar beating pattern.

7

Fig. 1. Experimental observation of sperm motion and their interactions with a curved wall. (A) The asymmetric sperm flagellar beating pattern over time, in which the thicker part of the flagellum always bends toward the left side of the sperm. (B) Image of a single sperm exhibiting intrinsic circular motion over time, acquired with phase contrast microscopy. As no twinkling was observed, it is apparent the sperm does not flip. (C) Trajectories of nine different sperm with intrinsic circular motion, in which no deterministic movement toward any direction was observed. (D) The sperm isolated within the quiescent medium feature either progressive (blue dashed line) or intrinsic circular motion (red dashed line). (E) Self-rolling motion in the swimmer results in a torque and subsequent swimming in circles. For $\Omega_R = 0$, no circular motion occurs. (F) Phase contrast microscopy enables us to differentiate the sperm with and without self-rolling. Rotation in the sperm head can be identified by it twinkling. Scale bar: 10 µm

142

143

144   Asymmetry in the flagellar beating pattern of sperm is shown to be reliant on the

145   intracellular Ca^{2+} concentration when it is exposed to a chemical stimulant (48, 49). For instance,

146   the biological pathway of asymmetric beating for some marine invertebrates in a gradient of

147   chemical stimulant, including *Ciona* and sea urchin, is known to involve Ca^{2+}-sensitive proteins

148   called "calaxin" (10) and "calmodulin" (48, 50, 51), respectively. The increase in the intracellular

149   concentration of Ca^{2+} leads to calaxin (or calmodulin) suppressing the movement of the outer

150   dynein arm. This suppression of the outer dynein arm then leads to asymmetric beating. Although

151   the role of calmodulin involved in the motility of stimulated sperm is known to be central for most

152   mammals (52) (e.g., bovine sperm (49)), the biological details of asymmetric beating at different

153   stages of sperm motility, including activated (i.e., unstimulated) and hyperactivated (i.e.,

154   stimulated) is still unknown. Therefore, further molecular insight into asymmetric beating in

155   mammalian sperm is required to propose a mathematical model at the single cell level that captures

156   the molecular details of the process. Nevertheless, several studies have been carried out to propose

157   potential mechanisms for in-plane sperm circular motion caused by asymmetric flagellar beating

158   for both unstimulated and stimulated sperm. A well-established method to connect the asymmetry

159   in the beating pattern of unstimulated sperm to its circular movement is to measure the intrinsic

160   flagellar curvature (41), so that a non-zero curvature in one beat yields a circular motion. This non-

161   zero curvature can be due to the compression of the sperm flagellum by the internal forces in a

162   viscous fluid, which results in a buckling behavior so that symmetry in the beating breaks and thus

163   the sperm swims in circular trajectories, as proposed by Gadelha et al. (53). Recently, Saggiorato

164   et al. (39) studied the motion of a progesterone-stimulated tethered human sperm and proposed

165   that a phase difference between the first and second harmonic yields a non-zero torque and thus

166   can lead to a circular motion of stimulated sperm. Although this study brings new insights about

167   the role of temporal harmonics in the beating pattern and its relation to the circular motion of

168   stimulated tethered human sperm, it is not necessarily valid for the untethered, unstimulated bovine

169   sperm in our study. Therefore, other potential mechanisms at the single cell level by which

170   asymmetric flagellar beating of untethered and unstimulated bovine sperm leads to circular

171   movement are required.

172   To determine the relation between asymmetric beating and circular motion of sperm, we

173   first reconstructed the beating patterns of the flagellum over one beat. We then applied the Fourier

174   transform to the beating pattern to yield its temporal frequencies (Supplementary Information Part

175   I). Our results indicate that asymmetry in the beating pattern is associated with an increase of the

176   main frequency (i.e., first harmonic) as well as decrease in its amplitude. Moreover, the zeroth and

177   higher harmonics simultaneously appear in the frequency domain as the asymmetry occurs. We

178   then described the beating pattern in the Fourier series ansatz, which includes an offset term as

179   well as the first and higher harmonics, as described in Eq. 1,

$$y(x,t) = \sum_{n=0} a_n cos(n\omega t - kx) \qquad (1)$$

180

181   in which $k = \frac{2\pi}{\lambda}$ (with $\lambda \approx L$) is the wave number, ω is the main frequency, and a_n is the amplitude

182   of the nth harmonic, including a non-thermal white Gaussian noise (54). That is, the amplitude can

183   be described by $a_n = \tilde{a}_n(1 + \eta_n(t))$ with $\langle \eta_n(t) \rangle = 0$ and $\langle \eta_n(t) \cdot \eta_{n'}(t') \rangle = D_n \delta_{nn'} \delta(t - t')$.

184   This non-thermal noise may stem from asynchrony in the collective dynamic (55–57) of the dynein

185   motor proteins that are responsible for transport along microtubules within the sperm flagella (3,

186   10).

187   Applying resistive force theory on the wave function described by Eq. 1, we can calculate

188   the forces produced by each segment of the flagellum in the tangential (x) and normal (y) directions

189   using $f_x = -(\xi_N - \xi_T)(\frac{\partial y}{\partial t})(\frac{\partial y}{\partial x})$ and $f_y = -\xi_N\left(\frac{\partial y}{\partial t}\right) + (\xi_N - \xi_T)(\frac{\partial y}{\partial t})(\frac{\partial y}{\partial x})^2$, in which ξ_N and ξ_T

190   are drag coefficients in the normal and tangential directions. Therefore, the time-averaged forces

191   produced by each segment of the flagellum in the tangential ($\tilde{f}_x$) and normal ($\tilde{f}_y$) directions can be

192   described by:

193
$$\tilde{f}_x = -\frac{1}{2}(\xi_N - \xi_T)\omega k \sum_{n=0} n\tilde{a}_n^2 \qquad (2)$$

194
$$\tilde{f}_y = (\xi_N - \xi_T)\omega k^2 a_0 sin(kx) \sum_{n=0} n\tilde{a}_n^2 \qquad (3).$$

195   Integrating $\tilde{f}_x$ and $\tilde{f}_y$ over the flagellum, the total forces produced in the tangential and normal

196   directions are $L\tilde{f}_x$ and zero, respectively. Although the emergence of the zeroth harmonic does not

197   lead to a net normal force and subsequent translational motion, it produces a torque

198
$$\tau_f = (\xi_N - \xi_T)\omega k L a_0 \sum_{n=0} n\tilde{a}_n^2 \qquad (4).$$

199   The obtained relations for the produced force and torque by the flagellum reveal that while the

200   tangential force is correlated to the characteristics of the first and higher harmonics, the amplitude

201   of the zeroth harmonic is involved in the torque as well. Applying the zero net torque and force

202   constraint, the tangential and angular velocity are found to be correlated through a_0:

203
$$\widetilde{\Omega} = \frac{\xi_T}{\xi_N}(\frac{24a_0}{L^2}\tilde{V}_p) \qquad (5)$$

204   in which $\widetilde{\Omega}$ is the average angular velocity (Supplementary Information Part II).

11

205   To validate the analysis, we experimentally measured the angle sperm sweeps out in one

206 beat ($\Delta\theta$), in which $\Delta\theta$ is the difference between the deviation of the sperm head direction from

207 the average path to its left (θ_1) and right (θ_2) sides (Fig. 2A). Fig. 2B displays the measured $\Delta\theta$

208 values for sperm with progressive motility and circular motion. As can be seen, the average of

209 $\Delta\theta(t)$ (i.e., $\widetilde{\Delta\theta}$) for sperm with circular movement are significantly higher than that of sperm with

210 progressive motility. Considering that $\widetilde{\Omega} = \frac{\omega}{2\pi} \cdot \widetilde{\Delta\theta}$, we measured the normalized angular velocity

211 ($L\widetilde{\Omega}V_p^{-1}$) and curvature of the sperm path ($\tilde{\kappa}L$) with regards to the amplitude of the zeroth

212 harmonic, as shown in Fig. 2C. Based on Fig. 2C, we determined $\frac{\xi_N}{\xi_T}$ to be 1.93 ± 0.33, which is

213 comparable to previously reported values (58). Based on these experimental results and the

214 agreement they show to the relations we derived from resistive force theory, we conclude that the

215 circular motion in the sperm motility is attributed to the zeroth harmonic in the flagellar beating.
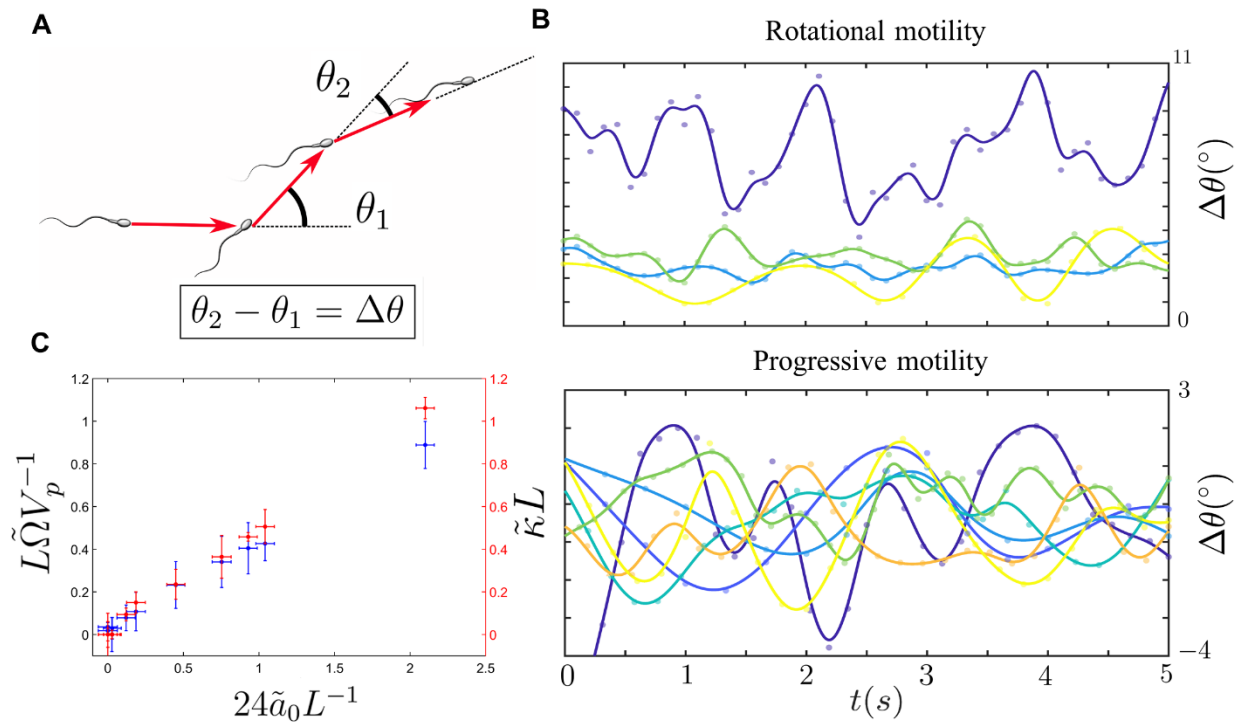
216

217

Fig. 2. Intrinsic circular motion caused by the presence of the zeroth harmonic. (A) Schematic of sperm motion featuring intrinsic circular motion. θ_1 and θ_2 are the deviation in the sperm direction towards the left and right of the mean path. (B) $\Delta\theta$ measured for sperm with circular motion (top) and progressive motility (bottom). The average value of $\Delta\theta$ is significantly higher in sperm with circular motion. (C) The normalized angular velocity ($L\widetilde{\Omega}V_p^{-1}$, blue) and curvature of the sperm path ($\tilde{\kappa}L$, red) plotted versus the amplitude of the zeroth harmonic ($\widetilde{a_0}$) to experimentally confirm the results obtained from resistive force theory. $\frac{\xi_N}{\xi_T}$ was determined to be 1.80 ± 0.34 and 2.07 ± 0.31 for the blue and red data points, respectively. The average of these values reported as $\frac{\xi_N}{\xi_T}$ in the main text.

218

219   We also demonstrate the effect of non-thermal Gaussian noise (33) in the amplitude of the

220   zeroth harmonic on the sperm trajectory. Based on the results gained from the resistive force theory

221   analysis, the noise in the zeroth harmonic yields a similar noise in the angular velocity. Therefore,

222   the angular velocity can be described as $\Omega = \widetilde{\Omega}(1 + \eta_0(t))$. Including the non-thermal white

223   Gaussian noise in the angular velocity and simulating the sperm motion at different signal-to-noise

224   ratios (SNR), we found that this noise leads to stochastic movement of the center of the sperm's

225   circular path, as can be seen in Fig. 3A, which is consistent with our experimental observation of

226   bull sperm movement shown in Fig. 1C. These findings suggest that the inconsistency in the

227   sperm's circular path is a consequence of the noise in the amplitude of the zeroth harmonic. In

228   addition, we found the sperm are more capable of maintaining their circular path at higher SNR

229   values (SNR = 50, 55, 60), and thus we observe less movement at the center of these paths, as can

230   be seen in Fig. 3A. At lower SNR values, the sperm motion contains more stochasticity and thus

231   covers a larger domain. We repeated the simulation for 1000 sperm cells to find the diffusivity of

232   the circular path's center (i.e., D_c) at different SNR values, and as can be seen in Fig. 3B, D_c is

233   inversely correlated to the SNR. Accordingly, we expect the distance of the circular path's center

234   from its initial location, $r_c(t)$ to increase over time with $(D_c t)^{0.5}$. Fig. 3C shows the $r_c(t)$ obtained

235   at different SNR values, which confirms the localization of the sperm at high SNR and the increase

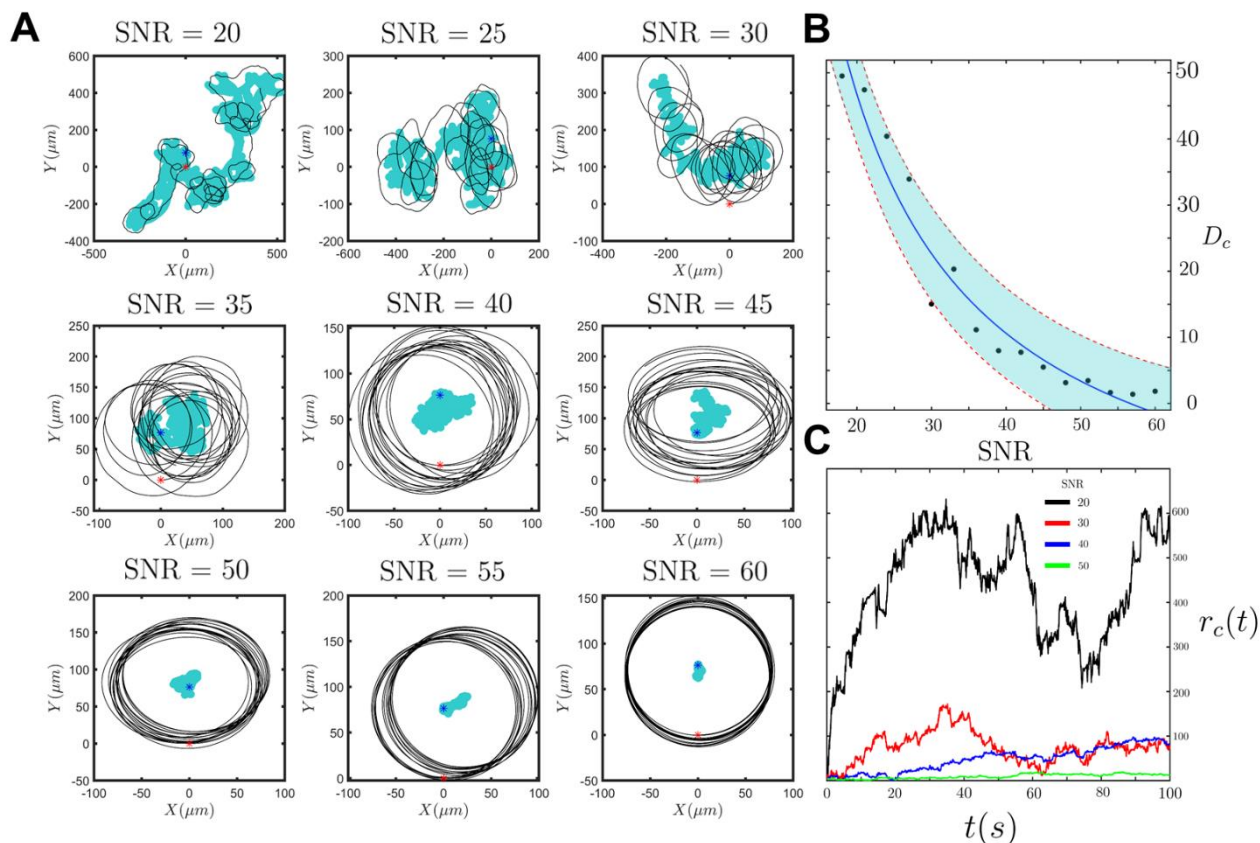236   of $r_c(t)$ in time with $t^{0.5}$.

Fig. 3. Noise in the angular velocity and the corresponding diffusivity of the circular path's center. (A) The sperm trajectory at 9 different signal-to-noise ratios ($20 \leq SNR \leq 60$). Higher SNR values yield more consistent and deterministic circular motion. (B) The diffusivity of the circular path's center vs. SNR. Each point in the figure was obtained by simulating the motion of 1000 sperm cells with similar initial conditions. (C) The distance of the circular path's center from its initial location with respect to time. The obtained results are at 9 different SNR; 4 of which are demonstrated in this figure.

237

238

239

240

241

15

242   Berke et al. (27) modeled the far-field approximation of the flow generated by a

243   microswimmer with progressive motion as a pusher force dipole. Therefore, we used the sperm

244   dipole model, including the components of the circular motion, to calculate the sperm contribution

245   to the fluid flow and thus the hydrodynamic interactions inside the quiescent zone at distances

246   adequately away from the curved sidewall ($> 2 \times$ sperm length). The proposed model is depicted

247   in Fig. 4A, in which f is the tangential force produced by the sperm flagellum, f'' is the

248   perpendicular force corresponding to the torque caused by asymmetric beating, and f' is the drag

249   force required for the torque-free condition (26). The magnitude of f' and f'' are equivalent to

250   each other while the $\frac{f''}{f}$ ratio (i.e., γ) is equal to $\frac{2\tilde{a}_0}{L}$ (see Eq. S38). The contribution of the sperm's

251   active swimming to the fluid flow is the solution of the Stokes equation for the proposed model

252   shown in Fig. 4A. The general form of the Stokes equation for such a swimmer is

253
$$\nabla p - \mu \nabla^2 v = \sum f_i \delta(r - r_i) \qquad (6)$$

254   in which p is the pressure, μ is the dynamic viscosity of the TALP medium (0.94 mPa/s), v is the

255   fluid velocity, r is the position, r_i is the position of the point force f_i, and δ is the Dirac delta

256   function. To solve the Stokes equation, we can either use Green's function, known as the

257   "Stokeslet" description (42, 59), or solve the equation numerically. The analytical expression for

258   the swimmer model using the Stokeslet description and mirror image (46, 60) method is explained

259   in Part IV of the Supplementary Information.

260   The near- and far-field flow produced by sperm has been studied previously (61). However,

261   for the sake of simplicity and precision, we carried out finite element method simulations in a

262   cylindrical domain similar to the quiescent zone to numerically solve the Stokes equation along

263   with mass conservation (62). Considering the sperm swim in a quasi-2D plane that is located ~5

16

264   μm below the top surface and parallel to it (63), we obtained the velocity field imposed by the

265   flagellar beating for $\widetilde{\Delta\theta} = 0° - 15°$ (Fig. 4B). We then integrated the net flow in the y direction

266   (Fig. 4B) imposed on the sperm body, which is caused by the presence of the no-slip walls, to

267   calculate the hydrodynamic interaction (i.e., HI), the results of which are demonstrated in Fig. 4C.

268   The velocity field generated by the progressive flagellar beating ($\widetilde{\Delta\theta} = 0$) in the presence of the

269   no-slip boundaries leads to the attractive hydrodynamic interactions (> 0), as indicated in Fig. 4C,

270   which agrees with previous studies (22). As we added and increased the components of the circular

271   motion, the attractive hydrodynamic interactions decayed for a constant progressive velocity of

272   the sperm (20 $\mu m/s$ $<V_p<$ 80 $\mu m/s$), indicating that the motion of the microswimmer is less

273   influenced by nearby boundaries as components of circular motion emerge in the motion. To gain

274   a better understanding about the mechanism of this reduction in hydrodynamic attraction, we

275   simulated the flow field produced by components of the progressive $(\vec{f})$ and the circular motion

276    $(\vec{f''}$ and $-\vec{f''})$ and their corresponding drags $(-\vec{f},\vec{f'}$ and $-\vec{f'})$ separately (Fig. S4). The flow field

277   produced by the progressive component and its corresponding drag is outward in the front and rear

278   of the swimmer, while inward on the sperm's right and left sides. In contrast, the flow field

279   produced by the components of the circular motion and their corresponding drags are inward in

280   the front and rear of the swimmer, while outward on the sperm's right and left sides. Accordingly,

281   as the components of the circular motion becomes larger, more of the flow imposed by the

282   progressive motion is damped by that of the circular motion and therefore the hydrodynamic

283   attraction decreases with sperm circular motion.

284   This decay in the far-field hydrodynamic interaction is also predicted by the analytical

285   expression for the swimmer model using the Stokeslet description. In fact, the attraction of the

17

286 sperm toward the wall in the presence of the components of the circular motion can be described

287 by:

$$u_y = u_y^p(-2 + 3cos(2\widetilde{\Delta\theta}) - \gamma sin(2\widetilde{\Delta\theta})) \qquad (7),$$

289 in which u_y and u_y^p describe the far-field attraction with and without the components of the circular

290 motion. Neglecting γ, an increase in $\widetilde{\Delta\theta}$ results in a decrease of attraction to the walls.

291 Interestingly, at $\widetilde{\Delta\theta}_n = \frac{1}{2}\cos^{-1}\frac{2}{3} \approx 24.1°$ and corresponding curvature of $\tilde{\kappa}_n = \frac{\omega}{4\pi\tilde{V}_p}\cos^{-1}\frac{2}{3}$, the

292 swimmer experiences no attraction toward the walls and becomes neutral.
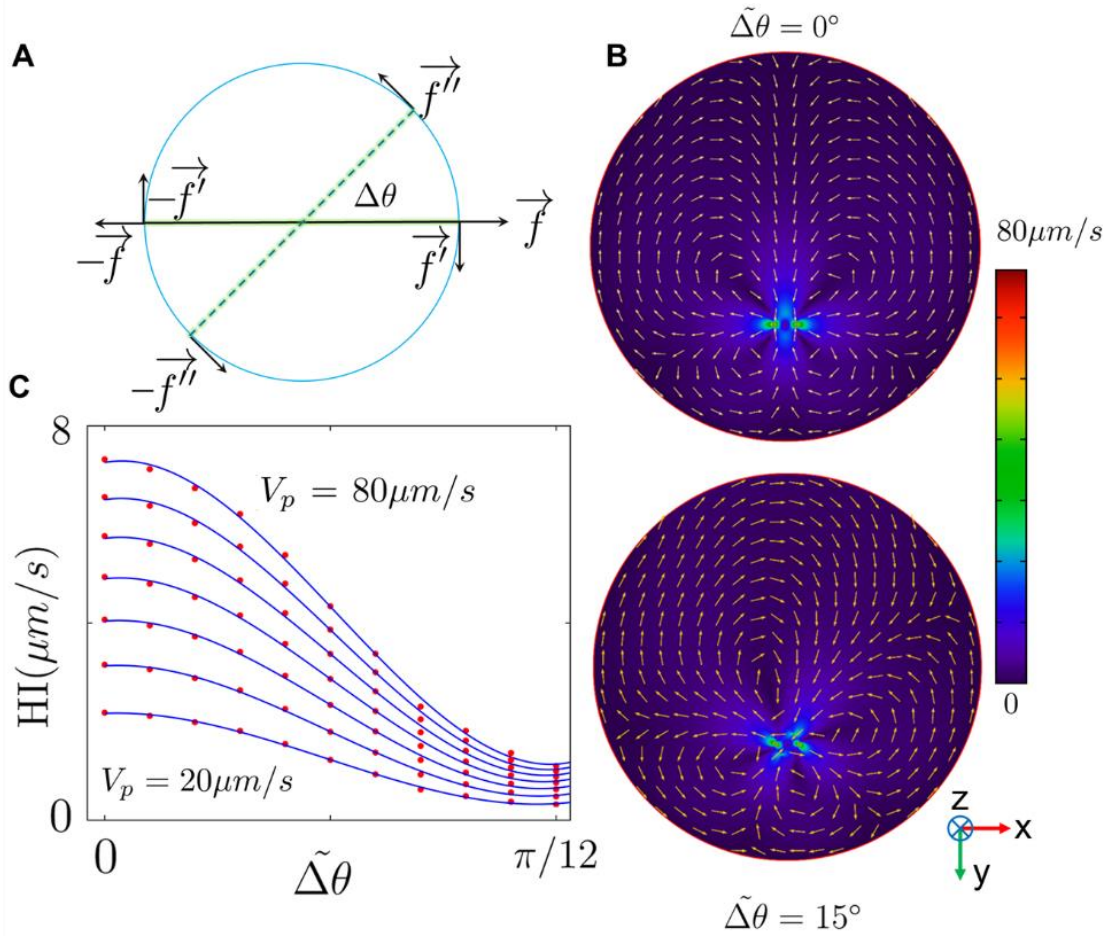
293

294

295

Fig. 4. Dipole swimmer model and far-field hydrodynamic interactions. (A) The dipole swimmer model, including the components of the circular motion (f' and f''). (B) The velocity field obtained from solving the Stokes equation for the dipole swimmer model in a quiescent medium. The colors represent the magnitude and the arrows are normalized to visualize the direction of the vector field. (C) The attraction caused by the presence of the wall decays as we increase $\Delta\theta$.

296

297

298

299

300

301   At the near-wall condition (< the sperm body length), the dipole approximation is no longer

302   valid (35) and the sperm-wall interaction can be understood by near-field approximations, as

303   previous theoretical (38, 64) and simulation-based (65) studies suggest. We categorize the sperm

304   interaction with the curved sidewall into four different types: 1) a progressive sperm encounters

305   the wall, rotates, and follows it, as can be seen in Fig. 5A(I); 2) a non-progressive sperm encounters

306   the wall, follows it temporarily, and detaches (Fig. 5A(II)); 3) a non-progressive sperm that does

307   not contact the wall (Fig. 5A(III)); and 4) a non-progressive sperm that encounters the wall and

308   stays still or moves slowly along it (Fig. 5A(IV)). These categories can be seen in Movie S2. To

309   interpret these near-wall interactions, we first used surface contact force analysis, in which the

310   wall influence on the sperm movement is modeled as a normal force.

311   When sperm is in contact with the wall surface there is a positive surface contact force,

312   whereas a surface force of zero corresponds to detachment of the swimmer from the wall (66).

313   Consider a sperm that encounters the wall of the quiescent zone with an incident angle of β, as

314   depicted in Fig. 5B. Under a zero-net force constraint, the normal surface force becomes $N =$

315    $F_T sin(\beta) - F_N cos(\beta)$, where F_T and F_N are the tangential and perpendicular forces, respectively.

316   The threshold angle that corresponds to the $N = 0$ situation (i.e., β_{th}) is equal to $\tan^{-1} \gamma$. For $\beta <$

317   β_{th}, the normal surface force becomes negative and no contact occurs accordingly. Hence, the

318   sperm does not follow the wall. Since an increase in γ leads to higher β_{th}, sperm with greater γ

319   values are less likely to contact and follow the wall.

320   For incident angles greater than β_{th} (where the sperm-wall contact occurs), an increase in

321   F_N leads to a smaller N, and thus easier detachment from the wall results. For the other condition,

322   in which the direction of the perpendicular force is opposite (Fig. 5C), the surface force becomes

323   greater ($N = F_T sin(\beta) + F_N cos(\beta)$) and detachment is more difficult. However, since the final

324   orientation of the swimmer at the contact point is tilted, the component of the perpendicular force

325   along the wall overcomes the tangential force, and subsequently the sperm movement along the

326   wall becomes slower. At the extreme condition, the sperm cell stands still.
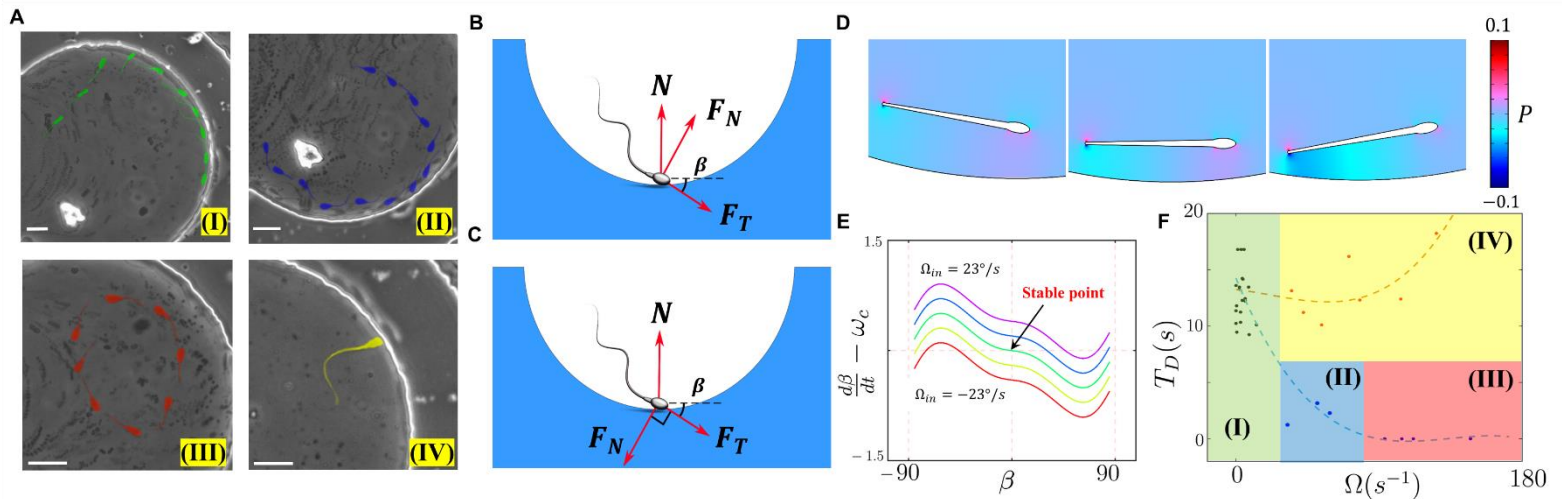
327

Fig. 5. Near-field interactions and the susceptibility of the sperm to follow the wall. (A) Sperm with (I) progressive motility that is susceptible to the wall, (II) low intrinsic circular motion and partial susceptibility to the wall, and (III) high intrinsic circular motion and zero susceptibility to the wall. A non-progressive sperm that encounters the wall and stays still is also depicted in (IV). Scale bar: $10\mu m$ (B) The forces produced by the sperm flagellum and the normal surface contact force (N). This arrangement describes Fig. A(I) and (II) and (III). (C) The forces produced by the sperm flagellum and the normal contact force. This arrangement describes Fig. A(IV). (D) The pressure distribution caused by sliding of sperm nearby the wall at $\beta = -20°, 0°,$ and $20°$, from left to right. This pressure distribution is used to calculate the torque and angular velocity imposed on the sperm by the presence of the wall. (E) Dynamic of the sperm incidence angle in the phase-plane, depicted at different intrinsic angular velocity values ($-23\,°/s \leq \Omega_{in} \leq 23\,°/s$). (F) The sperm detention time on the curved wall measured for sperm with different intrinsic angular velocities. Sperm with $|\Omega_{in}| > 76°/s$ (red box) do not contact the wall, while the ones with $8° \leq |\Omega_{in}| \leq 76°$ (blue box) are partially susceptible to the wall and follow it temporarily. Sperm with $|\Omega_{in}| \leq 8°$ (green box) are capable of following the wall without detaching. The detention time for sperm cells corresponding to (IV) in Fig. 5(A) and Fig. 5(C) are presented in the yellow box.

328

329

330   Although surface contact force analysis can be used to gain a general notion of near-field

331   interactions, its only valid under circumstances where contact occurs. Therefore, we also

332   developed a hydrodynamic explanation for near-field interactions to obtain more quantitative

333   characterization. We used lubrication theory as a platform, where the sperm distance from the wall

334   was assumed to be much smaller than its length (42). We then solved the Stokes equation and

335   extracted the pressure distribution for sperm (Fig. 5D) at different incident angles ($-90° < \beta <$

336    $90°$) and constant progressive velocity ($V_p = 80 \ \mu m/s$). Given that the contribution of pressure in

337   the stress tensor dominates that of the viscous stress (42) ($pI \gg \mu(\nabla v + \nabla v^T)$), the torque exerted

338   by the wall was calculated and the corresponding angular velocity is

339
$$\frac{d\beta}{dt} = \frac{1}{\xi_N} \frac{\int \sigma(x - x_{cm}) \, dx}{\int (x - x_{cm})^2 dx} \qquad (8) \, ,$$

340   in which σ is the stress tensor and x_{cm} is the coordinate of the sperm's center of mass. The obtained

341   angular velocity as a function of β, including the effect of Ω_{in}, is shown in Fig. 5E. As can be seen

342   in Fig. 5E, for $\Omega_{in} = 0$, the stable point occurs at $\beta = 0$ with $\frac{d\beta}{dt} = \omega_c$, which is the required

343   angular velocity to follow the boundary of the curved wall (Supplementary Information part IV).

344   Whereas for $\Omega_{in} > 0$, which corresponds to the configuration of Fig. 5B, $\frac{d\beta}{dt} > \omega_c$ at $\beta = 0$,

345   meaning it is not stable when following the boundary and the sperm subsequently detaches from

346   the wall. For $\Omega_{in} < 0$ (Fig. 5C), $\frac{d\beta}{dt} - \omega_c = 0$ at $\beta < 0$, which results in the tilted orientation of

347   the sperm at its contact point, and thus harder detachment and slower boundary-following motion.

348   To confirm our results obtained from the surface force analysis and lubrication

349   approximation, we experimentally measured the time of sperm detention on the wall (i.e., T_D) for

350   different Ω_{in} (Fig. 5F). The experimental results for T_D indicate that the sperm exhibiting intrinsic

351 circular motion either do not contact the wall ($|\Omega_{in}| > 76°/s$) or swim on the wall for shorter

352 times ($8°/s < |\Omega_{in}| < 76°/s$) compared to progressive sperm, which is consistent with the

353 findings of the surface force analysis. The detention time for sperm cells corresponding to (IV) in

354 Fig. 5(A) and Fig. 5(C) are presented in the yellow box in Fig. 5(F), which confirms that the

355 components of the circular motion in sperm can lead to higher detention times and harder

356 detachments, as we anticipated. Based on these experimental data, and similar to the far-field case,

357 sperm with progressive motility are the most susceptible to near-field boundary-dependent

358 navigation.

359 By isolating sperm cells based on their rheotactic behavior using a microfluidic system, we

360 demonstrated that sperm cells are able to navigate via upstream swimming while they feature a

361 continuum of asymmetry in their flagellar beating patterns. To identify the role of asymmetric

362 beating on the boundary-dependent navigation, and then compare it to rheotaxis, we then

363 investigated sperm motion after isolation in a quiescent zone with curved walls. Our results

364 indicate that asymmetric flagellar beating patterns cause sperm to swim in circles. This circular

365 motion of the sperm the far-field hydrodynamic interactions so that sperm with intrinsic circular

366 motion are less attracted to walls. Likewise, at distances closer to the wall, the sperm with non-

367 progressive motility are less likely to navigate along the wall in comparison to completely

368 progressive sperm.

369 Based on these results, we conclude that boundary-dependent navigation is more sensitive

370 to the beating pattern compared to sperm rheotaxis; whereas sperm rheotaxis is more sensitive to

371 the motility (VAP). Accordingly, the findings of this paper, accompanied with the clinical

372 correlation between fertility and progressive motility in sperm samples (67), suggests that at some

373 points during the fertilization process, boundary-dependent navigation plays a central role. The

374   findings of this study provide a comprehensive understanding of sperm locomotion during the

375   fertilization process before reaching the fertilization site and thus can be used to improve the

376   conventional tools for infertility diagnosis and treatment (68).

377   **Materials and Methods**

378   **Semen sample preparation.** Commercially available cryopreserved bovine semen samples were

379   kindly provided by Genex Cooperative (Ithaca, NY) in milk and egg yolk-based extender in plastic

380   straws. The semen in the straws were thawed in a 37 ℃ water bath and then diluted 1:3 with TALP

381   (the sperm culture medium). After dilution, the viscosity of the samples was ~2.1 mPa s^{-1}. The

382   initial sperm concentration in the semen samples were ~100 million/mL and after diluting with

383   TALP, reduced to a quarter of the initial concentration. The motility of the semen sample after

384   dilution ranged from 20–30%. We used 10 different semen samples in both milk and egg yolk-

385   based extender. The TALP recipe was as follows: NaCl (110 mM), KCl (2.68 mM), NaH$_2$PO$_4$

386   (0.36 mM), NaHCO$_3$ (25 mM), MgCl$_2$ (0.49 mM),CaCl$_2$ (2.4 mM), Hepes buffer (25 mM), glucose

387   (5.56 mM), pyruvic acid (1.0 mM), penicillin G (0.006% or 3 mg/500 ml), and bovine serum

388   albumin (20 mg/ml).

389   **Micro fabrication process and semen injection.** The microfluidic device was made of

390   polydimethylsiloxane using a standard soft lithography protocol (69, 70). The diameter of the

391   curved quiescent zone was 200 µm and the height of the chamber was 25 µm. The diluted semen

392   was injected into the microfluidic device using gravitation and the flow generated in the channel

393   was controlled by changing the height of the semen container. Since sperm rheotaxis emerges

394   under very low shear rate (0.6 s^{-1}), using gravitation instead of conventional syringe pumps is a

395   more efficient way to obtain and control low flow rates.

396   **Rheotaxis-based sperm isolation and phase-contrast microscopy.** To isolate motile bovine

397   sperm inside the quiescent zone, we utilized a microfluidic corral system(40) that isolates motile

398   swimmers based on their ability to move upstream. As we injected the sample with an injection

399   rate of 1.2 mL/h, sperm with motilities higher than 53.2 µm/s can swim upstream and enter the

400   quiescent zone (which is filled with TALP), allowing us to study the sperm movement with

401   minimal fluid mechanical noise. The movement of the sperm cells were acquired with a phase-

402   contrast microscope, where flipping of the sperm head leads to subsequent phase shifts in the light

403   passing through, leading to variation in the observed brightness (i.e., a twinkling effect).

404   **Cell tracking and zeroth harmonic measurement.** The sperm trajectories and other motility

405   related characteristics were analyzed with ImageJ and a custom MATLAB code. To measure the

406   amplitude of the zeroth harmonic, we measured the maximum amplitude of the beating towards

407   the left (y_L) and right (y_R) sides of the swimmer, so that the magnitude of the zeroth harmonic is:

408
$$a_0 = \frac{|y_L - y_R|}{2} \qquad (9).$$

409   The error bars in Fig. 2(C) result from measuring a_0 at 10 different beats, while the error bars of

410     $\widetilde{\Omega}$ and $\tilde{\kappa}$ in the same figure were obtained from 10 circles of movement.

411   **Numerical simulation**

412   **Beating pattern reconstruction.** To reconstruct the beating pattern of the sperm, we posited the

413   temporal part of the flagellar beating could be described by two Sine and Cosine function defined

414   on the interval of $[\pi - \phi_0, \phi_0]$ so that $\phi_0 \in [\pi, 2\pi]$. Later, by evenly extending the function (71),

415   we obtained the beating patterns so that ϕ_0 determines the asymmetry in the beating; e.g. $\phi_0 = 2\pi$

416   corresponds to completely symmetric beating and thus progressive motility, while $\phi_0 < 2\pi$ results

25

417   in asymmetry. We then applied a fast Fourier transform on the beating patterns to determine their

418   temporal frequencies. These steps were performed using MATLAB (version R2017a).

419   **Finite element method simulations.** To obtain the velocity field imposed by the dipole swimmer

420   model and determine the far-field hydrodynamic interactions, we first imported the structure of

421   the quiescent zone in the COMSOL MULTIPHYSICS (version 5.2) platform. Two orthogonal

422   Gaussian pulse functions (defined in the x and y directions) were used to define each point force

423   in the dipole swimmer model. The mathematical form of the pulse is a 2D Gaussian distribution

424
$$f\delta(x - x_0)\delta(y - y_0) = \frac{f}{2\pi\sigma_x\sigma_y}e^{\frac{-(x-x_0)^2}{2\sigma_x^2}}e^{\frac{-(y-y_0)^2}{2\sigma_y^2}}$$ (9).

425   We use x_0, y_0 to move and σ_x, σ_y to focus the point forces arbitrarily. This strategy was chosen to

426   lower the computational costs and prevent issues related to using small volumetric forces and their

427   associated meshing problems in the finite element method. Finally, solving the Stokes and mass

428   conservation equations for different $\Delta\theta$ values, we obtained the results demonstrated in Fig. 4B.

429   Then by integrating the velocity field imposed by the sperm, we obtained the hydrodynamic

430   interactions in the y direction, as shown in Fig. 4C.

431   To find the torque imposed on the sperm at near-field through the lubrication

432   approximation, we first solved the Stokes equation for the schematic shown in Fig. 5D at different

433   incident angles. Exporting the pressure distribution and assuming the sperm's center of mass was

434   located on the flagellum and twice closer to the head than to the tail, the torque imposed by the

435   wall on the sperm and the subsequent angular velocity were calculated.

26

444

445   **References**

446   1.   Yanagimachi R (1994) Mammalian fertilization. *Physiol Reprod*.

447   2.   Suarez SS, Pacey AA (2006) Sperm transport in the female reproductive tract. *Hum*

448   *Reprod Update* 12(1):23–37.

449   3.   Shiba K, Baba SA, Inoue T, Yoshida M (2008) Ca2+ bursts occur around a local minimal

450   concentration of attractant and trigger sperm chemotactic response. *Proc Natl Acad Sci*

451   105(49):19312–19317.

452   4.   Jikeli JF, et al. (2015) Sperm navigation along helical paths in 3D chemoattractant

453   landscapes. *Nat Commun* 6:7985.

454   5.   Friedrich BM, Jülicher F (2007) Chemotaxis of sperm cells. *Proc Natl Acad Sci*

455   104(33):13256–13261.

456   6.   Bahat A, et al. (2003) Thermotaxis of mammalian sperm cells: a potential navigation

457   mechanism in the female genital tract. *Nat Med* 9(2):149.

458   7.   Tung C, et al. (2015) Microgrooves and fluid flows provide preferential passageways for

459   sperm over pathogen Tritrichomonas foetus. *Proc Natl Acad Sci* 112(17):5431–5436.

460 8.   Kantsler V, Dunkel J, Blayney M, Goldstein RE (2014) Rheotaxis facilitates upstream

461   navigation of mammalian sperm cells. *Elife* 3.

462 9.   Miki K, Clapham DE (2013) Rheotaxis guides mammalian sperm. *Curr Biol* 23(6):443–

463   452.

464 10. Mizuno K, et al. (2012) Calaxin drives sperm chemotaxis by Ca2+-mediated direct

465   modulation of a dynein motor. *Proc Natl Acad Sci* 109(50):20497–20502.

466 11. Kaupp UB, et al. (2003) The signal flow and motor response controling chemotaxis of sea

467   urchin sperm. *Nat Cell Biol* 5(2):109.

468 12. Gray J, Hancock GJ (1955) The propulsion of sea-urchin spermatozoa. *J Exp Biol*

469   32(4):802–814.

470 13. Alvarez L, et al. (2012) The rate of change in Ca2+ concentration controls sperm

471   chemotaxis. *J Cell Biol* 196(5):653–663.

472 14. Wadhams GH, Armitage JP (2004) Making sense of it all: bacterial chemotaxis. *Nat Rev*

473   *Mol cell Biol* 5(12):1024.

474 15. Strünker T, et al. (2011) The CatSper channel mediates progesterone-induced Ca 2+ influx

475   in human sperm. *Nature* 471(7338):382.

476 16. Demott RP, Suarez SS (1992) Hyperactivated sperm progress in the mouse oviduct. *Biol*

477   *Reprod* 46(5):779–785.

478 17. Suarez SS (1987) Sperm transport and motility in the mouse oviduct: observations in situ.

479   *Biol Reprod* 36(1):203–210.

28

480 18. Tulsiani D (2012) *Introduction to mammalian reproduction* (Springer Science & Business
481   Media).

482 19. Suarez SS (2016) Mammalian sperm interactions with the female reproductive tract. *Cell
483   Tissue Res* 363(1):185–194.

484 20. Denissenko P, Kantsler V, Smith DJ, Kirkman-Brown J (2012) Human spermatozoa
485   migration in microchannels reveals boundary-following navigation. *Proc Natl Acad Sci*
486   109(21):8007–8010.

487 21. Zaferani M, Palermo GD, Abbaspourrad A (2019) Strictures of a microchannel impose
488   fierce competition to select for highly motile sperm. *Sci Adv* 5(2):eaav2111.

489 22. Elgeti J, Kaupp UB, Gompper G (2010) Hydrodynamics of sperm cells near surfaces.
490   *Biophys J* 99(4):1018–1026.

491 23. Tung C, et al. (2015) Emergence of upstream swimming via a hydrodynamic transition.
492   *Phys Rev Lett* 114(10):108102.

493 24. Bukatin A, Kukhtevich I, Stoop N, Dunkel J, Kantsler V (2015) Bimodal rheotactic
494   behavior reflects flagellar beat asymmetry in human sperm cells. *Proc Natl Acad Sci*
495   112(52):15904–15909.

496 25. Elgeti J, Gompper G (2009) Self-propelled rods near surfaces. *EPL (Europhysics Lett*
497   85(3):38002.

498 26. Li G (2016) Hydrodynamics of swimming microorganisms in complex fluids. Dissertation
499   (Purdue University).

500 27. Berke AP, Turner L, Berg HC, Lauga E (2008) Hydrodynamic attraction of swimming

501   microorganisms by surfaces. *Phys Rev Lett* 101(3):38102.

502   28.   Nosrati R, Graham PJ, Liu Q, Sinton D (2016) Predominance of sperm motion in corners.

503   *Sci Rep* 6:26669.

504   29.   Baskaran A, Marchetti MC (2009) Statistical mechanics and hydrodynamics of bacterial

505   suspensions. *Proc Natl Acad Sci* 106(37):15567–15572.

506   30.   Brotto T, Caussin J-B, Lauga E, Bartolo D (2013) Hydrodynamics of confined active

507   fluids. *Phys Rev Lett* 110(3):38101.

508   31.   Li G, Tang JX (2009) Accumulation of microswimmers near a surface mediated by

509   collision and rotational Brownian motion. *Phys Rev Lett* 103(7):78101.

510   32.   Schaar K, Zöttl A, Stark H (2015) Detention times of microswimmers close to surfaces:

511   Influence of hydrodynamic interactions and noise. *Phys Rev Lett* 115(3):38101.

512   33.   Ma R, Klindt GS, Riedel-Kruse IH, Jülicher F, Friedrich BM (2014) Active phase and

513   amplitude fluctuations of flagellar beating. *Phys Rev Lett* 113(4):48101.

514   34.   Drescher K, Dunkel J, Cisneros LH, Ganguly S, Goldstein RE (2011) Fluid dynamics and

515   noise in bacterial cell--cell and cell--surface scattering. *Proc Natl Acad Sci*

516   108(27):10940–10945.

517   35.   Li G-J, Ardekani AM (2014) Hydrodynamic interaction of microswimmers near a wall.

518   *Phys Rev E* 90(1):13010.

519   36.   Takatori SC, Yan W, Brady JF (2014) Swim pressure: stress generation in active matter.

520   *Phys Rev Lett* 113(2):28103.

521   37.   Guidobaldi A, et al. (2014) Geometrical guidance and trapping transition of human sperm

522   cells. *Phys Rev E* 89(3):32720.

523   38.   Spagnolie SE, Moreno-Flores GR, Bartolo D, Lauga E (2015) Geometric capture and

524   escape of a microswimmer colliding with an obstacle. *Soft Matter* 11(17):3396–3411.

525   39.   Saggiorato G, et al. (2017) Human sperm steer with second harmonics of the flagellar

526   beat. *Nat Commun* 8(1):1415.

527   40.   Zaferani M, Cheong SH, Abbaspourrad A (2018) Rheotaxis-based separation of sperm

528   with progressive motility using a microfluidic corral system. *Proc Natl Acad*

529   *Sci*:201800819.

530   41.   Friedrich BM, Riedel-Kruse IH, Howard J, Jülicher F (2010) High-precision tracking of

531   sperm swimming fine structure provides strong test of resistive force theory. *J Exp Biol*

532   213(8):1226–1234.

533   42.   Kim S, Karrila SJ (2013) *Microhydrodynamics: principles and selected applications*

534   (Courier Corporation).

535   43.   Lauga E, DiLuzio WR, Whitesides GM, Stone HA (2006) Swimming in circles: motion of

536   bacteria near solid boundaries. *Biophys J* 90(2):400–412.

537   44.   Hu J, Wysocki A, Winkler RG, Gompper G (2015) Physical sensing of surface properties

538   by microswimmers--directing bacterial motion via wall slip. *Sci Rep* 5:9586.

539   45.   Lemelle L, Palierne J-F, Chatre E, Vaillant C, Place C (2013) Curvature reversal of the

540   circular motion of swimming bacteria probes for slip at solid/liquid interfaces. *Soft Matter*

541   9(41):9759–9762.

542   46.   Di Leonardo R, Dell'Arciprete D, Angelani L, Iebba V (2011) Swimming with an image.

543   *Phys Rev Lett* 106(3):38101.

544   47.   Saleh B (2011) *Introduction to subsurface imaging* (Cambridge University Press).

545   48.   Brokaw CJ, Nagayama SM (1875) Modulation of the Asymmetry of Sea Urchin Sperm

546   Flagellar Bending by Calmodulin. (35):1875–1883.

547   49.   Ignotz GG, Suarez SS (2005) Calcium / Calmodulin and Calmodulin Kinase II Stimulate

548   Hyperactivation in Demembranated Bovine Sperm 1. 526(May):519–526.

549   50.   Smith EF (2002) Regulation of Flagellar Dynein by Calcium and a Role for an Axonemal

550   Calmodulin and Calmodulin- dependent Kinase. 13(September):3303–3313.

551   51.   Freya B, et al. (2018) Direction of flagellum beat propagation is controlled by proximal /

552   distal outer dynein arm asymmetry. 115(31). doi:10.1073/pnas.1805827115.

553   52.   Suarez SS (2008) Control of hyperactivation in sperm. *Hum Reprod Update* 14(6):647–

554   657.

555   53.   Gadêlha H, Gaffney EA, Smith DJ, Kirkman-Brown JC (2010) Nonlinear instability in

556   flagellar dynamics: a novel modulation mechanism in sperm migration? *J R Soc Interface*

557   7(53):1689–1697.

558   54.   Friedrich BM, Jülicher F (2009) Steering chiral swimmers along noisy helical paths. *Phys*

559   *Rev Lett* 103(6):68102.

560   55.   Shingyoji C, Higuchi H, Yoshimura M, Katayama E, Yanagida T (1998) Dynein arms are

561   oscillating force generators. *Nature* 393(6686):711.

562   56.   Ueno H, Yasunaga T, Shingyoji C, Hirose K (2008) Dynein pulls microtubules without

563   rotating its stalk. *Proc Natl Acad Sci* 105(50):19702–19707.

564   57.   Wang Q, et al. (2018) Molecular mechanisms of the interhead coordination by interhead

565   tension in cytoplasmic dyneins. *Proc Natl Acad Sci* 115(40):10052–10057.

566   58.   Elgeti J, Winkler RG, Gompper G (2015) Physics of microswimmers—single particle

567   motion and collective behavior: a review. *Reports Prog Phys* 78(5):56601.

568   59.   Yeomans JM, Pushkin DO, Shum H (2014) An introduction to the hydrodynamics of

569   swimming microorganisms. *Eur Phys J Spec Top* 223(9):1771–1785.

570   60.   Mathijssen AJTM, Pushkin DO, Yeomans JM (2015) Tracer trajectories and displacement

571   due to a micro-swimmer near a surface. *J Fluid Mech* 773:498–519.

572   61.   Ishimoto K, Gadêlha H, Gaffney EA, Smith DJ, Kirkman-Brown J (2017) Coarse-graining

573   the fluid flow around a human sperm. *Phys Rev Lett* 118(12):124501.

574   62.   Bruus H *Theoretical microfluidics. 2008* (New York: Oxford University Press).

575   63.   Nosrati R, Driouchi A, Yip CM, Sinton D (2015) Two-dimensional slither swimming of

576   sperm within a micrometre of a surface. *Nat Commun* 6:8703.

577   64.   Wysocki A, Elgeti J, Gompper G (2015) Giant adsorption of microswimmers: duality of

578   shape asymmetry and wall curvature. *Phys Rev E* 91(5):50302.

579   65.   Rode S, Elgeti J, Gompper G (2018) Sperm motility in modulated microchannels. *New J

580   Phys*.

581   66.   Kleppner D, Kolenkow R (2013) *An introduction to mechanics* (Cambridge University

582   Press).

583   67.   Guzick DS, et al. (2001) Sperm morphology, motility, and concentration in fertile and

584   infertile men. *N Engl J Med* 345(19):1388–1393.

585   68.   Hirano Y, et al. (2001) Andrology: Relationships between sperm motility characteristics

586   assessed by the computer-aided sperm analysis (CASA) and fertilization rates in vitro. *J*

587   *Assist Reprod Genet* 18(4):215–220.

588   69.   Azizi M, et al. (2018) Nanoliter-Sized Microchamber/Microarray Microfluidic Platform

589   for Antibiotic Susceptibility Testing. *Anal Chem* 90(24):14137.

590   70.   Azizi M, Zaferani M, Cheong SH, Abbaspourrad A Pathogenic Bacteria Detection Using

591   RNA-Based Loop-Mediated Isothermal-Amplification-Assisted Nucleic Acid

592   Amplification via Droplet Microfluidics. *ACS sensors*.

593   71.   Oppenheim A V (1999) *Discrete-time signal processing* (Pearson Education India).

594

595

596

597

598

599

600

601

602

603

604   Supplementary Information

605 **Effect of flagellar beating pattern on sperm rheotaxis and boundary-**
606 **dependent navigation**

607   Meisam Zaferani[1], Farhad Javi[1], Amir Mokhtare[1], Alireza Abbaspourrad[1]†

608   [1] Department of Food Science, College of Agriculture and Life Sciences, Cornell University,

609   Ithaca, NY, 14850, USA

610   † Corresponding author: alireza@cornell.edu

611 **I.   Reconstruction of sperm beating patterns and Fourier analysis**
612
613 To model beating patterns that resemble that of the sperm flagella, we studied the pattern in one

614 cycle of flagellar beating using a traveling sine wave with a temporal phase of $\phi(t) = \omega t$ (with

615 $\omega = 40\pi$ Hz as the angular frequency) in the range of $\pi - \phi_0 \leq \phi(t) \leq \phi_0$ so that $\phi_0 \in [\pi, 2\pi]$.

616 In turn, we constructed the even extension of the partial sine wave to form the flagellar beating

617 function over time. Fig. S1 shows these constructed patterns, which resemble the flagellar beating

618 of the sperm observed inside the quiescent zone. Here, the completely symmetric beating ($\phi_0 =$

619 2π) corresponds to sperm with absolute progressive motion, while asymmetry within the flagellum

620 motion ($\phi_0 < 2\pi$) results in intrinsic circular motion. To analyze the beating patterns and the

621 resulting sperm motion, we applied the Fourier transform to yield the temporal frequencies (Fig.

622 S2). Interestingly, with increasing temporal asymmetry in the beating pattern, the frequency of the

623 main (first) harmonic increases while its amplitude decreases. Moreover, the zeroth and second

624 harmonics simultaneously appear in the frequency domain.
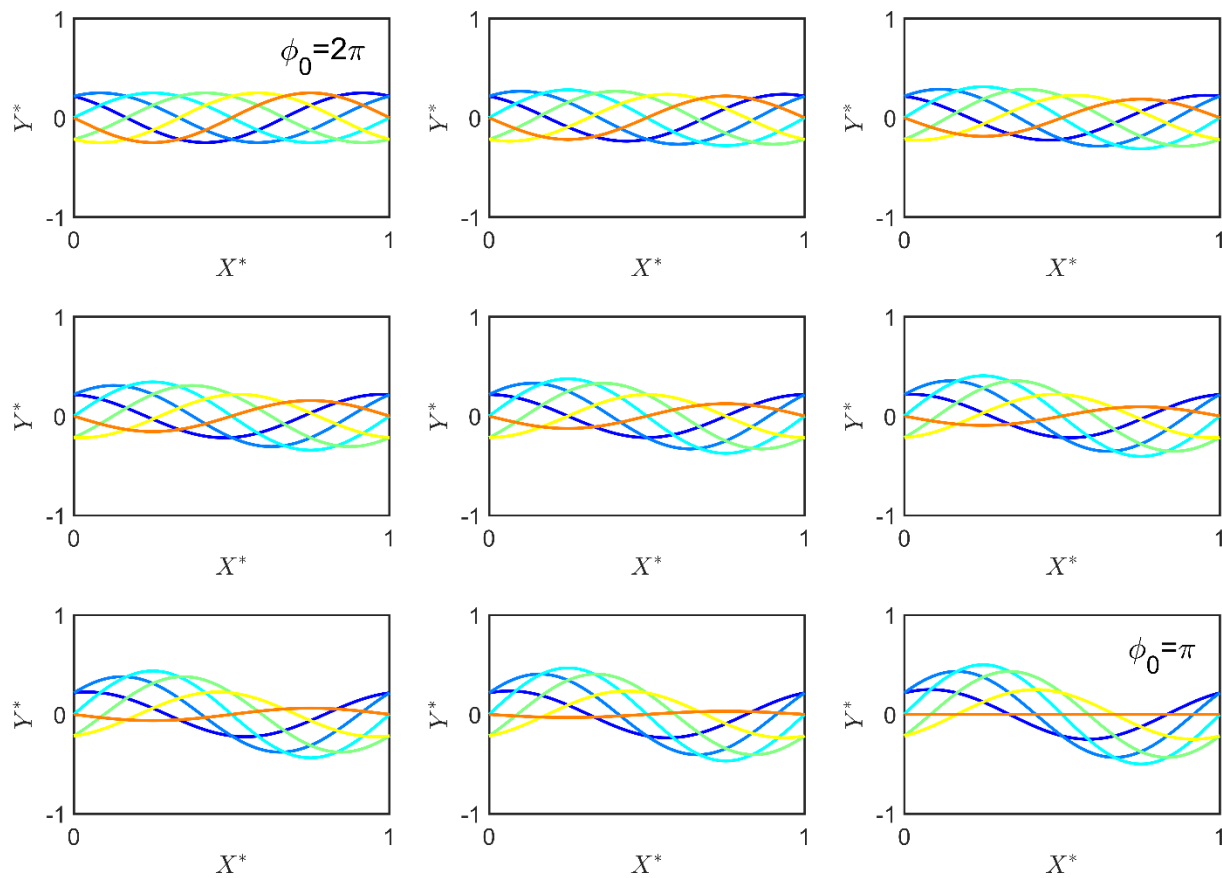
625

Fig. S1. The beating pattern of the sperm flagellum. The $\phi_0 = 2\pi$ situation corresponds to symmetric beating, and thus absolute progressive motility. As ϕ_0 decreases, asymmetry in the beating emerges and the motility includes a circular motion. x^* and y^* are normalized x and y axes as the sperm motion can be described in 2D Cartesian system.
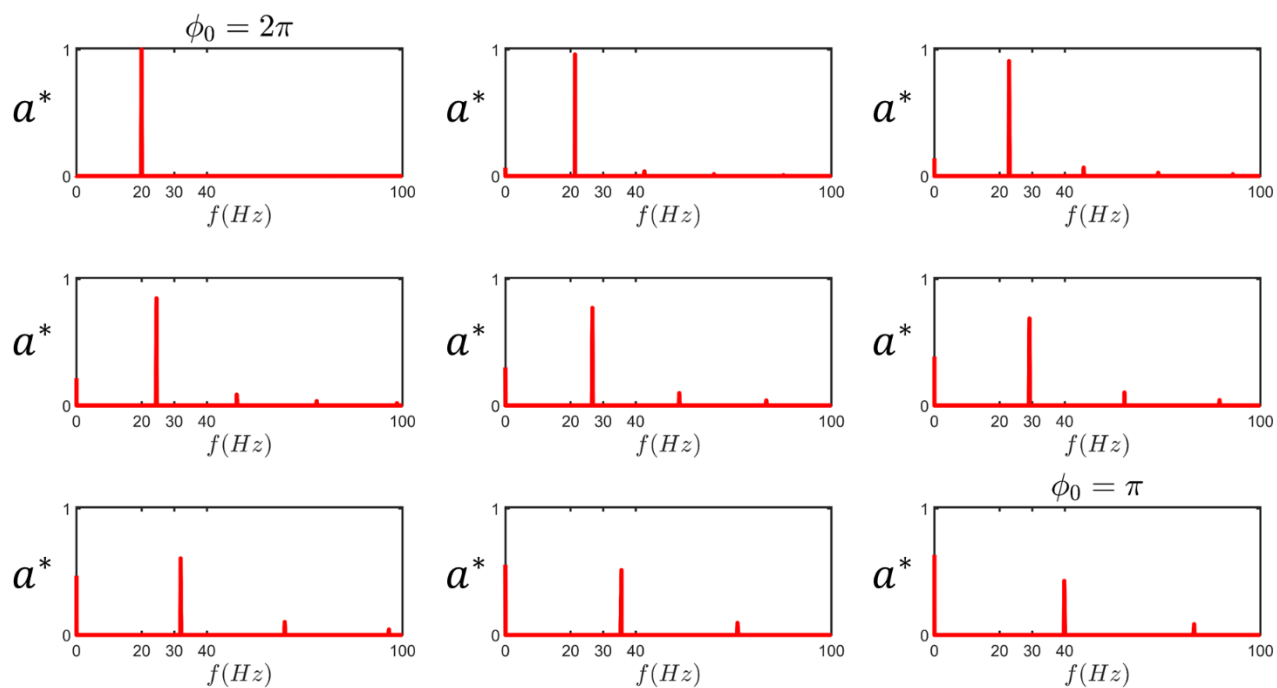
626

627

628

629

630

631

632

633

Fig. S2. The harmonics of the sperm beating. At $\phi_0 = 2\pi$, the beating pattern comprises a single frequency equal to 20 Hz. As asymmetry emerges in the beating, the main frequency shifts and higher harmonics along with the zeroth harmonic appear in the spectrum. a^* is the normalized amplitude of the harmonics.

634

635

636

637

638

639

640

641

642

643

644　**II. Resistive force theory**

645　In this section we use resistive force theory to derive equations describing the forces produced by

646　each segment of the flagellum and follow the presentation by Friedrich *et al*. (ref 41) and

647　Saggiorato *et al*.(ref 39). The velocity of each segment in the y direction (V) can be decomposed

648　into its tangential and normal components, V_T and V_N, using α, which is the tangential angle (S1–

649　4).

650
$$V = \frac{\partial y}{\partial t} \qquad (S1).$$

651
$$V_T = V \sin \alpha \qquad (S2)$$

652
$$V_N = V \cos \alpha \qquad (S3)$$

653
$$\tan \alpha = \frac{\partial y}{\partial x} \qquad (S4)$$

654　Relying upon resistive force theory, the forces produced by each element in the tangential and

655　normal directions are linearly related to the velocity in those directions:

656
$$f_T = -\xi_T V_T \qquad (S5)$$

657
$$f_N = -\xi_N V_N \qquad (S6).$$

658　In which, ξ_T and ξ_N are drag coefficients in the tangential and normal directions. Since the

659　amplitude of all harmonics are small in comparison to the sperm length, we can make the following

660　assumptions:

661
$$\forall n, a_n \ll L \rightarrow \tan \alpha \approx \sin \alpha \approx \alpha \qquad (S7)$$

662
$$\cos \alpha \approx \left(1 - \frac{\alpha^2}{2}\right) \qquad (S8).$$

663　Using the approximations in Eq. S7–8, we can write out the tangential and normal velocities and

664　forces using Eq. S9–12.

665
$$V_T \approx \left(\frac{\partial y}{\partial t}\right)\left(\frac{\partial y}{\partial x}\right) \qquad (S9)$$

666
$$V_N \approx \left(\frac{\partial y}{\partial t}\right)\left(1 - \frac{1}{2}\left(\frac{\partial y}{\partial x}\right)^2\right) \qquad (S10)$$

667
$$f_T = -\xi_T \left(\frac{\partial y}{\partial t}\right)\left(\frac{\partial y}{\partial x}\right) \qquad (S11)$$

668
$$f_N = -\xi_N \left(\frac{\partial y}{\partial t}\right)\left(1 - \frac{1}{2}\left(\frac{\partial y}{\partial x}\right)^2\right) \qquad (S12)$$
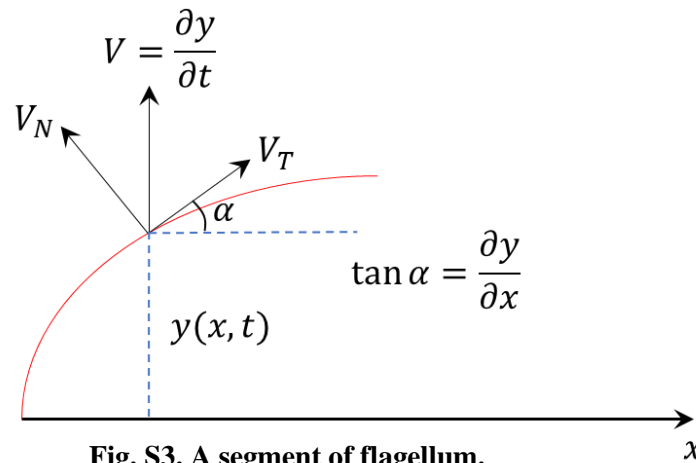
669

670

671

672

673

674

675

676

677

Fig. S3. A segment of flagellum.

678

679   The force produced by each segment in the x and y directions are described by Eq. S13–14.

680
$$f_x = f_T \cos\alpha - f_N \sin\alpha \qquad (S13)$$

681
$$f_y = f_T \sin\alpha + f_N \cos\alpha \qquad (S14)$$

682   Plugging Eq. S7, 11–12 into Eq. S13–14:

683
$$f_x = -\xi_T \left(\frac{\partial y}{\partial t}\right)\left(\frac{\partial y}{\partial x}\right)\left(1 - \frac{1}{2}\left(\frac{\partial y}{\partial x}\right)^2\right) + \xi_N \left(\frac{\partial y}{\partial t}\right)\left(\frac{\partial y}{\partial x}\right)\left(1 - \frac{1}{2}\left(\frac{\partial y}{\partial x}\right)^2\right) \quad (S15)$$

684
$$f_y = -\xi_T \left(\frac{\partial y}{\partial t}\right)\left(\frac{\partial y}{\partial x}\right)^2 + -\xi_N \left(\frac{\partial y}{\partial t}\right)\left(1 - \frac{1}{2}\left(\frac{\partial y}{\partial x}\right)^2\right)\left(1 - \frac{1}{2}\left(\frac{\partial y}{\partial x}\right)^2\right) \qquad (S16),$$

685   yields Eq. S17–18, which are the forces produced by the flagellum in the x and y directions.

686
$$f_x = -(\xi_N - \xi_T)\left(\frac{\partial y}{\partial t}\right)\left(\frac{\partial y}{\partial x}\right) \qquad (S17)$$

687
$$f_y = -\xi_N \left(\frac{\partial y}{\partial t}\right) + (\xi_N - \xi_T)\left(\frac{\partial y}{\partial t}\right)\left(\frac{\partial y}{\partial x}\right)^2 \qquad (S18)$$

688

689 **III.   Force and Torque produced by the flagellum**

690 **1. Force in the x direction**

691 The forces produced by a segment of flagellum moving with $y(x,t)$ in the tangential and normal

692 directions can be described by Eq. S17 and S18, where ξ_T and ξ_N are the corresponding drag

693 coefficients. Plugging Eq. S19 into Eq. S17 yields Eq. S20.

694
$$y(x,t) = \sum_{n=0} a_n cos(n\omega t - kx) \quad (S19)$$

695
$$f_x = (\xi_N - \xi_T)\left(\sum_{n=0} a_n(n\omega)\sin(n\omega t - kx)\right)\cdot\left(\sum_{n=0} -a_n k \sin(n\omega t - kx)\right) \quad (S20)$$

696
$$f_x = -k\omega(\xi_N - \xi_T)\left(\sum_{i,j} i a_i a_j \sin(i\omega t - kx)\sin(j\omega t - kx)\right) \quad (S21)$$

697 For $i \neq j$, the time average of f_x would be zero, thus we only retain terms with $i = j$. This yields

698 Eq. S22–23.

699
$$f_x = -k\omega(\xi_N - \xi_T)\left(\sum_{n=1} n a_n{}^2 \sin^2(i\omega t - kx)\right) \quad (S22)$$

700
$$f_x = -\frac{1}{2}k\omega(\xi_N - \xi_T)\left(\sum_{n=1} n a_n{}^2(1 - \cos 2(i\omega t - kx))\right) \quad (S23)$$

701 By calculating the time average of Eq. S23, the average force produced by each segment of the

702 flagellum in the x direction can be described by Eq. S24.

703
$$\tilde{f}_x = \frac{1}{T}\int_0^T f_x \, dt = -\frac{1}{2}k\omega(\xi_N - \xi_T)\sum_{n=1} n\tilde{a}_n{}^2 \quad (S24)$$

704 Integrating the $\tilde{f}_x$ over the flagellum, the total force and velocity produced in the x direction is:

705
$$\tilde{F}_x = L\tilde{f}_x = -\frac{1}{2}k\omega L(\xi_N - \xi_T)\sum_{n=1} n\tilde{a}_n{}^2 = -\xi_T \tilde{V}_p L \rightarrow \tilde{V}_p = \frac{1}{2}k\omega\left(\frac{\xi_N}{\xi_T} - 1\right)\sum_{n=1} n\tilde{a}_n{}^2 \quad (33).$$

40

706 **2. Force in the y direction and the corresponding torque**

707 Plugging Eq. S19 into Eq. S18 yields Eq. S25.

708
$$f_y = -(\xi_N - \xi_T)\left(\sum_{n=0} a_n(n\omega)\sin(n\omega t - kx)\right) \cdot \left(\sum_{n=0} a_n k \sin(n\omega t - kx)\right)^2 \qquad (S25)$$

709
$$f_y = -k^2\omega(\xi_N - \xi_T)\left(\sum_{n=0} n a_n \sin(n\omega t - kx)\right) \cdot \left(\sum_{i,j} a_i a_j \sin(i\omega t - kx)\sin(j\omega t - kx)\right) \quad (S26)$$

710 One can write out Eq. S26 in the form of Eq. S27.

711
$$f_y = -k^2\omega(\xi_N - \xi_T)\left(\sum_{n,i,j} n a_n a_i a_j \sin(n\omega t - kx)\sin(i\omega t - kx)\sin(j\omega t - kx)\right) \qquad (S27)$$

712 Since we are interested in time average values of f_y, the following terms of Eq. S27 are non-zero:

713
$$i = 0, j = n$$

714
$$j = 0, i = n$$

715 Therefore, Eq. S27 reduces to Eq. S28–29:

716
$$f_y = -2a_0 k^2 \omega(\xi_N - \xi_T)\sin(-kx)\left(\sum_n n a_n^2 \sin^2(n\omega t - kx)\right) \qquad (S28).$$

717
$$f_y = a_0 k^2 \omega(\xi_N - \xi_T)\sin(kx)\left(\sum_n n a_n^2(1 - \cos2(n\omega t - kx))\right) \qquad (S29)$$

718 Taking the average of Eq. S28, the average force produced by each segment in the y direction is:

719
720
$$\widetilde{f_y} = \frac{1}{T}\int_0^T f_y \, dt = (\xi_N - \xi_T)\omega k^2 a_0 sin(kx)\sum_{n=0} n\tilde{a}_n^2 \qquad (S30).$$
721

722   Interestingly, but not surprisingly, the force produced by each segment of the flagellum in the y

723   direction is a function of x, meaning that the effect of the zeroth harmonic can be seen in the force

724   produced in the y direction.

725   Integrating the forces produced by each segment in the y direction over the flagellum, the total

726   force produced in the y direction becomes zero:

727
$$\tilde{F}_y = \int_0^L \tilde{f}_y\, dx = 0 \qquad (S31).$$

728   However, the total force produced in the front half of the sperm is non-zero and equal to the force

729   produced in the rear half of the sperm:

730
$$\tilde{F}_{yF} = \int_0^{\frac{L}{2}} \tilde{f}_y\, dx = 2(\xi_N - \xi_T)\omega k a_0 \sum_{n=0} n\tilde{a}_n{}^2 \qquad (S32)$$

731
$$\tilde{F}_{yB} = -2(\xi_N - \xi_T)\omega k a_0 \sum_{n=0} n\tilde{a}_n{}^2 \qquad (S33).$$

732   We calculated these two forces for the γ ratio, which is required for the Stokeslet description of

733   the microswimmer model. Although the total force produced in the y direction is zero, the torque

734   produced by the flagellum is not zero:

735
$$\tau_f = \int (x - x_{CM})\tilde{f}_N dx = (\xi_N - \xi_T)\omega k L \tilde{a}_0 \sum_N n\tilde{a}_n{}^2 \qquad (S34).$$

736   To find the angular velocity of the sperm $\tilde{\Omega}$, we need to calculate the torque produced by drag as

737   well:

738
$$\tau_d = -\int (x - x_{CM})^2 \xi_N \tilde{\Omega} dx = -\xi_N \tilde{\Omega} \frac{L^3}{12} \qquad (S35).$$

739   Considering the zero net-torque condition, we can simply find the angular velocity of the sperm:

42

740

$$\tau_f + \tau_d = 0 \rightarrow \tilde{\Omega} = \frac{12\,(\xi_N - \xi_T)\omega k L \tilde{a}_0}{\xi_N L^3} \sum_N n \tilde{a}_n{}^2 = \frac{\xi_T}{\xi_N}\left(\frac{24\tilde{a}_0}{L^2}\tilde{V}_p\right)\ (S36).$$

743

744 Since the curvature of the sperm trajectory is described by $\tilde{\Omega}\tilde{V}_p^{-1}$ (in which $\tilde{\Omega}$ is the angular

745 velocity of the sperm and $\tilde{V}_p$ is the sperm velocity), the curvature can be defined as:

746

747
$$\tilde{\kappa} = \frac{\tilde{\Omega}}{\tilde{V}_p} = \frac{24\tilde{a}_0}{L^2}\left(\frac{\xi_T}{\xi_N}\right) \qquad (S37).$$

748

749 In turn, one can write out the γ ratio as:

$$\gamma = \frac{\tilde{F}_{NF}}{2\tilde{F}_T} = \frac{2a_0}{L} \qquad (S38)$$

752

753

754

755

756

757

758

759

760

761

762

763

43

764 **IV.   The analytic solution for the swimmer model using the Stokeslet description**

765 The velocity field imposed by a source point is known as the Stokeslet (Eq. S39), i.e., the most

766 fundamental solution for the Stokes equation. Based on the linearity in the Stokes equation, the

767 contribution of the actively swimming sperm on the fluid flow can be described by superimposing

768 the flow fields produced by each point force. For the sake of simplicity, we write out the imposed

769 velocity field in three terms, including:

770   1) The velocity field imposed by $\vec{f}$ and $-\vec{f}$ (Eq. S40),

771   2) $\vec{f'}$ and $-\vec{f'}$ (Eq. S41), and

772   3) $\vec{f''}$ and $-\vec{f''}$ (Eq. S42). In which the magnitude of $\vec{f'}$ and $\vec{f''}$ are equal to $\gamma\vec{f}$.

773
$$\vec{u}_f = \frac{1}{8\pi\mu}\left\{\frac{\vec{f}}{r} + \frac{(\vec{f}.\vec{r})\vec{r}}{r^3}\right\} \qquad (S39)$$

774
$$\vec{u}_{\{f,-f\}} = \vec{u}_f + \vec{u}_{-f} = \frac{p\vec{r}}{8\pi\mu r^3}\{-1 + 3\cos^2\varphi\} \qquad (S40)$$

775
$$\vec{u}_{\{f',-f'\}} = \frac{1}{8\pi\mu r^3}\left\{\vec{f'}rd\cos\varphi - f'r\sin\varphi\vec{d} + \frac{3rd\cos\varphi}{r^2}f'r\sin\varphi\vec{r}\right\} \qquad (S41)$$

776
$$\vec{u}_{\{f'',-f''\}} = \frac{1}{8\pi\mu r^3}\left\{\vec{f''}rd'\cos(\varphi+\Delta\theta) - f''r\sin(\varphi+\Delta\theta)\vec{d'} - \frac{3}{2}f''d'\sin(2\varphi+2\Delta\theta)\right\} \quad (S42)$$

777 Using Eq. S40, S41, and S42, the velocity field imposed by the swimmer model is:

778
$$\vec{u}_T = \frac{p}{8\pi\mu r^2}\left\{A\hat{r} + (\bar{\bar{I}}\cos(\varphi) - \bar{\bar{B}}\cos(\varphi+\Delta\theta))\gamma\hat{f'} - (\bar{\bar{I}}\sin(\varphi) - \bar{\bar{B}}\sin(\varphi+\Delta\theta))\gamma\hat{d}\right\} \qquad (S43)$$

779 with

780
$$A = -1 + 3\cos^2\varphi + \frac{3}{2}\left(\sin(2\varphi) - \sin(2\varphi+2\Delta\theta)\right)$$

781 $\bar{\bar{B}} = \begin{bmatrix} \cos\Delta\theta & -\sin\Delta\theta \\ \sin\Delta\theta & \cos\Delta\theta \end{bmatrix}$ and $\bar{\bar{I}} = \begin{bmatrix} 1 & 0 \\ 0 & 1 \end{bmatrix}$.

782

44

783   The influence of the no-slip boundary condition on the imposed flow is modeled by the mirror

784   image of the swimmer in the boundary. Accordingly, the velocity field imposed on the sperm that

785   causes the far-field attraction toward the wall is u_T with $r = 2h$, in which h is the distance between

786   the sperm and the wall. For $\varphi = \pi/2$, $A = -1 + \frac{3}{2}cos(2\Delta\theta)$,

787

$$u_y = \frac{p}{32\pi\mu h^2}\left\{1 - \frac{3}{2}cos(2\Delta\theta) + \frac{\gamma}{2}sin(2\Delta\theta)\right\} \qquad (S44)$$

788   is the attractive velocity field imposed on the swimmer by the wall. This equation can also be

789   written out as:

790

$$u_y = u_y^p\left(-2 + 3cos(2\widetilde{\Delta\theta}) - \gamma sin(2\widetilde{\Delta\theta})\right) \qquad (S45).$$

791   Interestingly, assuming $\gamma \ll 3$, at $\widetilde{\Delta\theta}_n = \frac{1}{2}cos^{-1}\frac{2}{3} \approx 24.1°$, the swimmer experiences no attraction

792   toward the walls and becomes neutral. Given the relation between $\widetilde{\Delta\theta}$, $\tilde{\kappa}$, and $\tilde{V}_p$, the corresponding

793   curvature that is inversely related to the progressive velocity is:

794

$$\tilde{\kappa}_n = \frac{\omega}{4\pi\tilde{V}_p}cos^{-1}\frac{2}{3} \qquad (S46).$$

795

796

797

798

799

800

801

802

803

45

804 **V.   The flow field produced by the progressive motility and circular motion.**

805   The flow field produced by the swimmer model in Fig. 4 is the superposition of the flow field

806   produced by the components of progressive motility $\left(\vec{f}\right)$ and circular motion $\left(\overrightarrow{f''} \text{ and } -\overrightarrow{f''}\right)$ and

807   their corresponding drags $\left(-\vec{f}, \overrightarrow{f'} \text{and} -\overrightarrow{f'}\right)$. To identify the mechanism of reduction in the far-field

808   attraction with the components of circular motion, we simulated the progressive term with

809   corresponding drag (Fig. S4(A)) and the components of circular motion with corresponding drags

810   (Fig. S4(B)), separately.   Similar to Fig. 4 in the manuscript, the arrows show the normalized

811   vector field while the magnitude of the flow is represented in color.
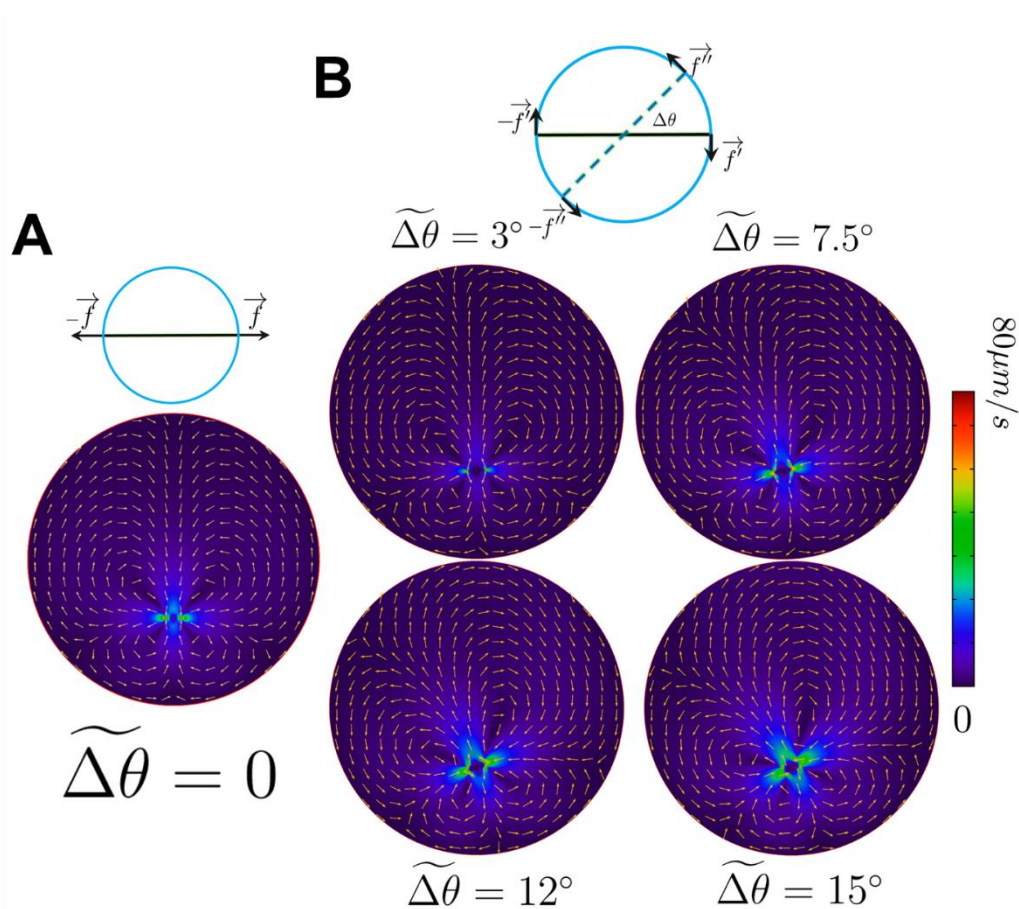
812

813

814

815

Fig. S4. The flow field produced by the components of the progressive motility and the circular motion. (A) The flow produced by the progressive component of motility and its corresponding drag. (B) The flow produced by the components of circular motion and their corresponding drags, $\Delta\theta$, ranging from 3° to 15°. The arrows are the normalized direction while the colors represent the magnitude of the velocity field.

816

817

818

819

820

47

821

VI. Lubrication approximation

823 The stress tensor is

824
$$\bar{\bar{\sigma}} = -p\bar{\bar{I}} + \mu(\nabla u^T + \nabla u) \qquad (S47).$$

825 At distances adequately close to the wall, the contribution of the pressure dominates and $\sigma \approx -p\bar{\bar{I}}$.

826 Accordingly, the torque exerted on the sperm by the boundary can be written out as

827
$$\tau = \int -p(x - x_{CM})dx \qquad (S48).$$

828 Neglecting the sperm mass, the net torque applied on the sperm is equal to zero, meaning that the

829 drag torque cancels out the torque exerted by the wall. This constraint gives us

830
$$\frac{d\beta}{dt} = \frac{1}{\xi_N} \frac{\int p(x - x_{CM})dx}{\int (x - x_{CM})^2} \qquad (S49),$$

831 in which β is the angle of the sperm swimming direction with respect to the wall.

832

833

48